Numerical Investigation of the Sediment Load Exchange between a Coastal Mud Bank and Its Neighbouring Estuary

Noelia Abascal-Zorrilla, Nicolas Huybrechts, Sylvain Orseau, Vincent Vantrepotte, Edward Anthony, Antoine Gardel

water

MDPI

Article

Numerical Investigation of the Sediment Load Exchange between a Coastal Mud Bank and Its Neighbouring Estuary

Noelia Abascal-Zorrilla [1], Nicolas Huybrechts [2,3,*], Sylvain Orseau [4], Vincent Vantrepotte [5], Edward Anthony [6] and Antoine Gardel [1]

[1] Centre National de la Recherche Scientifique-CNRS, UG, IFREMER (LEEISA URS 3456), Centre de Recherche de Montabo, 97334 Cayenne, France
[2] Cerema, RHITME Research Team, 134 rue de Beauvais, 60200 Compiegne, France
[3] Univ Rouen Normandie, Université Caen Normandie, CNRS, Normandie Univ, M2C UMR 6143, F-60280 Margny Lès Compiègne, France
[4] Setec Hydratec, 3 Chemin des Gorges de Cabriès, 13127 Vitrolles, France
[5] Laboratoire d'Océanologie et de Géosciences, Université du Littoral-Côte-d'Opale, CNRS, Université de Lille, IRD, 32 Avenue Foch, 62930 Wimereux, France
[6] Aix Marseille University, CNRS, IRD, INRAE, Coll France, CEREGE UM34, 13545 Aix-en-Provence, France
* Correspondence: nicolas.huybrechts@cerema.fr

Abstract: Muddy coastlines cover much of the world's shores, yet studies on the interaction between mud-affected coasts and estuaries are limited. This study focuses on the Mahury River estuary and its interaction with the muddy coast of the Guianas, primarily fed by the Amazon. A coupled wave–current–sediment transport model is developed to analyze the sediment exchange in an environment with strong interactions between the waves and the fluid mud. Simulations explore how seasonal changes in waves, mud availability, and tides affect sediment fluxes. The main processes influencing suspended particulate matter (SPM) and sediment transport are well emulated, notwithstanding the complexity of the ambient muddy environment. The results show that during the rainy season, strong wave damping and wave refraction zones cause high SPM resuspension in shallow waters (<5 m). In contrast, during the dry season, wave influence shifts to the estuary mouth. Erosion and sedimentation patterns indicate that ebb currents associated with neap tides during the rainy season represent the most favourable conditions for the alongshore migration of mud banks. Neaptide ebb currents also contribute to sedimentation during the dry season but only in the estuary mouth and the nearby coastal area. The abundance of mud leads to an extension of the estuary's intertidal area during the dry season.

Keywords: mud banks; estuary; numerical modelling; wave damping; sedimentary processes

Citation: Abascal-Zorrilla, N.; Huybrechts, N.; Orseau, S.; Vantrepotte, V.; Anthony, E.; Gardel, A. Numerical Investigation of the Sediment Load Exchange between a Coastal Mud Bank and Its Neighbouring Estuary. *Water* **2024**, *16*, 2885. https://doi.org/10.3390/w16202885

Academic Editors: Francois Marin and Nizar Abcha

Received: 30 August 2024
Revised: 27 September 2024
Accepted: 30 September 2024
Published: 11 October 2024

1. Introduction

Muddy coastal environments are mainly located between 30° N and 30° S of latitude [1–4]. Although estuaries are an important component of the dynamics in these muddy coastal areas, the general research effort has been concentrated on the transit of fluvial mud through estuaries and the interaction with the ambient environment (e.g., [5–7]). Many muddy coastal environments are, however, characterized by mud streaming alongshore, which tends to introduce complexity into the exchanges of suspended sediment with estuaries lying in the pathway of these mud streams [8–10]. This is notably the case of coasts affected by mud banks or high muddy suspensions streaming alongshore. The finest example is, without adoubt, the Amazon-influenced Guianas coast of South America. Located between Amapá (Brazil) and the Paria Peninsula (Venezuela), the Guianas exhibit the longest muddy shoreline (1500 km) in the world, characterized by the presence of mud banks migrating alongshore from the mouths of the Amazon to those of the Orinoco. The large supply of mud from the Amazon has dominated the geological development

of this coast. The mud exiting from the Amazon streams alongshore to the northwest as highly turbid suspensions (>1 g/L) before forming mud banks near the mouth of the Oyapock River at the border between Brazil and French Guiana, which migrate along the Guianas coast [11–16]. In any year, there are generally about 15 mud banks between the Amazon and the Orinoco, spaced 15–25 km apart. Their migration speed oscillates between 1 and 5 km/yr [17,18]. The banks are up to 5 m thick, 10 to 60 km long, and 20 to 30 km wide [12,19]. Waves are important in controlling mud bank dynamics and overall migration due to the strong interaction between the near-bed sediment transport and the wave propagation characteristics in the presence of mud [20,21].

Wave damping due to muddy coastal bedshas also been observed in other locations, such as central Jiangsu coast in China [22,23] or on the Atchafalaya Shelf, USA [24]. The particularity of the Guiana shoreline lies in the huge dimension of the coastal bank.

Incoming waves are damped by the presence of a thick layer of fluid mud in the leading edge of mud banks, whereas waves can propagate up to the shoreline on the consolidated seabed that characterizes the back of mud banks [20,25]. However, wind forcing, tidal currents, the North Brazil Current (NBC), and freshwater discharge also influence the migration process [16,26]. Mud banks constitute an important source of the fine sediment that enters the estuaries lying in the pathway of these alongshore-migrating banks [27]. Up to now, research on the interactions between such estuaries and this highly muddy, Amazon-influenced, coastal environment has been limited [25,28,29].

Between 2012 and 2018, a mud bank migrated across the mouth of the Mahury River (river catchment area: 3650 km^2), in the estuary of which the commercial port of French Guiana is located. Ref. [28] conducted various field surveys to characterize the hydrology and sediment dynamics of this estuary during the dry and the rainy season. Field surveys were also carried out on the adjacent subtidal parts of the muddy coastal area in order to determine its decadal-scale evolution and inter-annual variations. Further, Ref. [18] developed an algorithm to monitor the migration of the subtidal part of this mud bank along the French Guiana coast using Landsat 8 images. Field data are still, however, limited in space and duration due to the difficult logistic conditions for field work on this coast [25,26,30]. Satellite images provide a map of the turbid plume every few days, but most of the images are not exploitable during the rainy season months due to a high cloud cover. Moreover, the space resolution is not yet sufficient to track plumes inside narrow estuaries. To circumvent these difficulties, numerical models have been used to describe the current and salinity patterns on the Guiana continental shelf [31,32] and those of the turbid plume around a schematic mud bank [33]. These models were based on finite difference techniques and relied on very sparse data for validation. The interaction between fluid mud and waves was approached in these models using the equation of [34], or, alternatively, an additional source term was integrated inside SWAN (Simulating Waves Nearshore) [21,35,36] or Wavewatch III [37] to represent wave damping due to fluid mud using the methodologies of [38,39]. Both of these approaches compute wave propagation on a fixed bottom without considering the tide and the sediment transport. In order to better address the challenges posed by the interaction between estuaries and migrating mud banks, a 2D coupled wave–current transport model is developed here as a complementary tool to in situ and remote sensing data. The main objective is to shed light on sediment transport dynamics, focusing on sediment fluxes and the influence of various hydrodynamic forces in the nearshore area of the Mahury. While a 2D model was chosen to streamline computation and effectively address the well-mixed nearshore zone, it also serves as an initial step in understanding the model's capabilities in coupling wave processes with morphodynamics in an environment where strong interactions between waves and fluid mud occur. Although this study focuses on the specific case of the Mahury estuary, the proposed methodology can be applied to other estuaries with muddy coastal banks, such as those along the Guiana coast [40], the Patos Lagoon, influenced by the Rio de la Plata [41], and the Bay of Bengal, influenced by the Ganges–Brahmaputra–Meghna Delta [42].

The model employs the formulation developed in [38] in the wave module together with cohesive sediment transport and associated evolving morphodynamics. The model analyses the seasonal variation in and the relative importance of tides and waves involved in sediment exchanges between the aforementioned 2012–2018 coastal mud bank and the mouth of the estuary. First, the main characteristics of the Mahury estuary and its coastal environment are briefly introduced, followed by a presentation of the available dataset used to build and validate the model. The modelling strategy is then presented in detail with the different modules involved and the studied flow configurations. In this highly seasonal environment, particular attention is paid to the seasonal variation in the wave regime and in mud availability and their interaction with the neap–spring tidal cycle.

2. Materials and Methods

2.1. Study Area

The Mahury estuary in eastern French Guiana (Figure 1a) is affected by the north–south movement of the Intertropical Convergence Zone (ITCZ) and is subject to a highly seasonal tropical-equatorial climate. The rainy season starts at the end of December and lasts until July, and the dry season lasts from August to December. Between 2014 and 2019, the Mahury had an average water discharge of 90 m^3/s. Discharge ranged considerably from 5 to 437 m^3/s, reflecting a marked seasonal imprint (Figure 1e). Like all the estuaries located downdrift of the mouths of the Amazon, the Mahury is strongly influenced by the latter [27,43]. The estuary is located only110 km northwest of the Cassiporé mud cape in Brazil, where mud banks are formed [12] (Figure 1a). The mouth of the Mahury has a funnel-shaped morphology [28]. Ref. [28] pointed out that saline stratification occurs at the mouth during the wet season and that the water column is well mixed during the dry season. Between the shoreline and the islands, the flow is generally well mixed. Some saline stratification induced by the Amazon plume can be observed further offshore [44]. Bed sediments are composed of sand and mud with clay mineral proportions similar to those characterizing the Amazon River [45], but bedrock outcrops are also present on the west side of the channel. Mud banks commonly generate silting of the estuary's navigation channel and especially impinge on the east bank [28]. The mud bank that migrated across the mouth between 2012 and 2018 had its subtidal portion located between the estuary mouth and Cayenne city in 2015 (Figure 1b). This subtidal part was characterized by shallow depths (Figure 1b) and fluid mud (bulk density $\leq$ 1250 km/m^3) [29].

The seasonal oscillation of the trade winds off the Guianas coast has an influence on the large-scale hydrodynamic context [46]. These winds converge towards the ITCZ and are onshore-directed from the northeast in the rainy season and offshore-directed from the south during the dry season, as the ITCZ moves towards its northernmost position (Figure 1f). Winds are mainly active from December to May during the bulk of the rainy season, with an average annual mean speed of 6.5 m/s (Figure 1f). The Guianas coast is exposed to the waves that are mainly generated by the trade winds from the northeast during the rainy season and that tend towards a more northerly approach, in the lee of the ITCZ, during the dry season (Figure 1c). The annual average significant wave height (Hs) is 1.5 m and the peak period (Tp) is 8.8 s (Figure 1c,d), but the pattern is distinctly seasonal, with an average Hs of 1.7 min in the rainy season and 1.2 m in the dry season (Figure 1c,d). Significant wave heights have tended to exhibit a decreasing trend since 2015, with averaged annual maximum values dropping from 3.4 m to 2.3 m after 2015.

Tidal and oceanic currents are important in driving the suspended sediment dynamics in the coastal waters of French Guiana [33].The tide is semi-diurnal, with average neap and spring ranges of about 1.1 and 2.2 m, respectively [47]. Tidal currents have velocities of up to 0.15 m/s in the coastal area [48] and shore-normal tidal currents can locally attain 0.45 m/s [32]. The latter are dominant in the inner shelf zone compared to longshore currents. On the outer shelf, flows are along-shelf and generated by large-scale geostrophic currents [32].

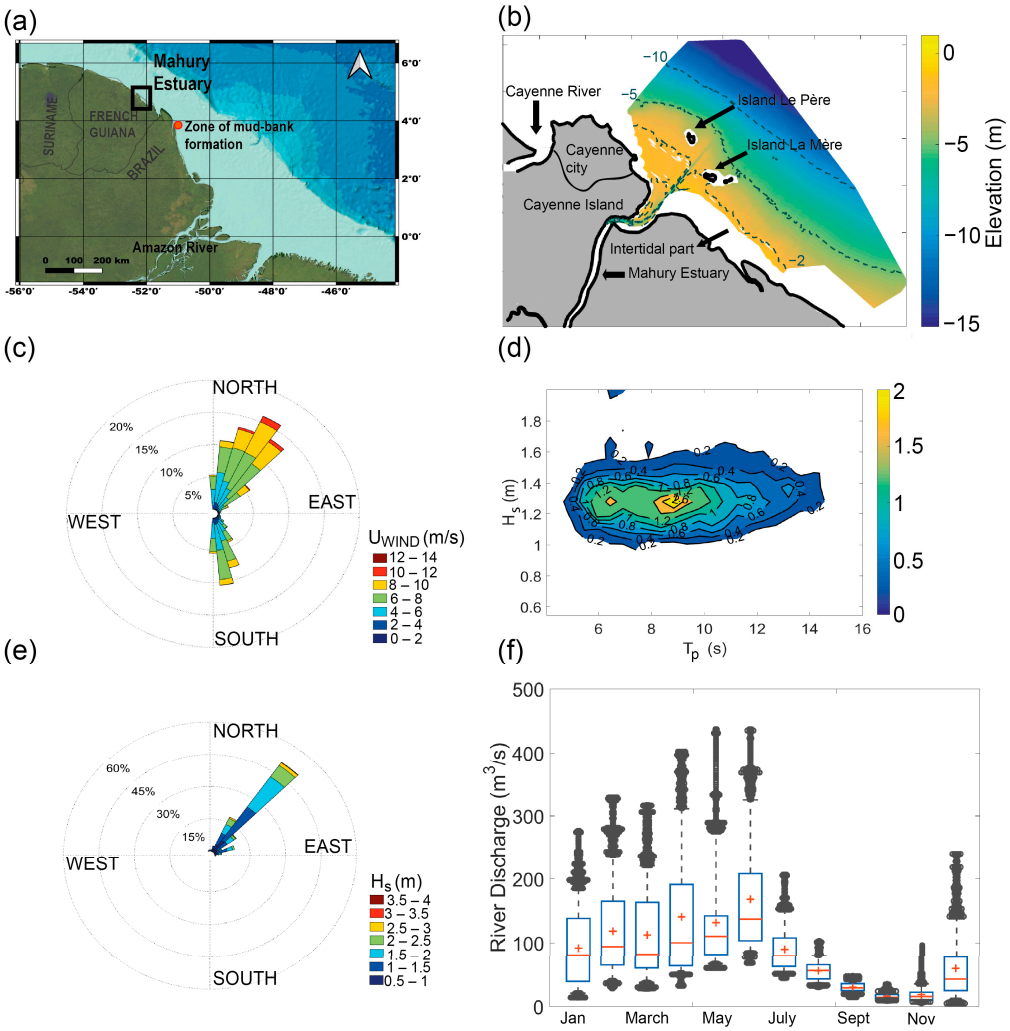

Figure 1. Setting and context of the Mahury River estuary: (**a**) location, (**b**) bathymetry of the coastal area and the mouth of the estuary in 2015 in the wake of migration of the mud bank across the latter, (**c**) wind rose, (**d**) significant wave height and period composition probability, (**e**) wave rose based on 7 years of wave data (buoy located at 20 m depth), and (**f**) mean(red cross), median (red line), 25th and 75th percentiles (blue box), extreme data points (whiskers extension), and outliers (black dots) of the annual cycle of monthly river discharge.

2.2. In Situ Measurements

Current velocities and turbidity were measured in two different points in the estuary: at stations S2 and Dégrad des Cannes (DDC) (Figure 2d). The survey at station DDC was conducted from 4 May to 19, during the rainy season of 2015. The S2 survey was also conducted during the rainy season, from 22 June to 6 July 2015. A multi-instrument bottom frame comprising a Nortek Aquadopp profiler (Nortek AS, Rud, Norway) (1 MHz) and a YSI EXO 2 multiparameter probe (Xylem Global, Washington, DC, USA) was deployed for both moorings at 0.55 m above the bed to avoid bed-level siltation. The adopted cell size for the Aquadopp profiler was 40 cm, and both instruments were configured with the same burst acquisition times of 10 s every 15 s. Velocity measurements were obtained at the water column, whereas turbidity was collected at the bottom. Turbidity measurements were calibrated using filtered values obtained following the same protocol as in [49], based on GF/F filters (0.7 µm pore size) using a linear relationship for the rainy season to obtain values of suspended particulate matter (SPM).

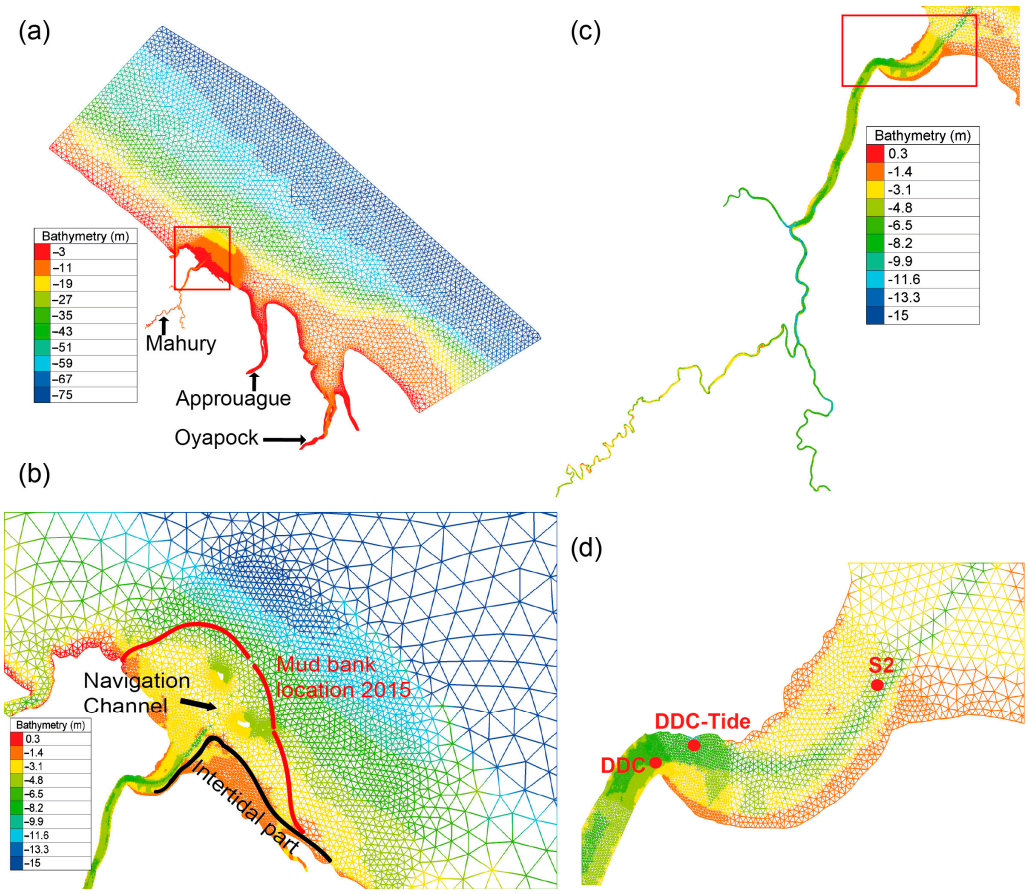

Figure 2. Mesh used for the hydro-sedimentary model. (**a**) Selected domain, (**b**) zoom on the Mahury estuary and the intertidal areas in 2015, where the navigation channel is clearly observed (values up to −8.5 m), (**c**) the Mahury River and its tributaries, (**d**) details of the mesh at the mouth of the estuary with the stations used to calibrate and validate the model (S2, DDC, and DDC-Tide).

Tide data were collected at the gauging station DDC-Tide (Figure 2d). Hourly river discharges were measured upstream of the limit of tidal influence. Although thisstudy focuses on the Mahury, other neighbouring estuaries influence the flow structures and there was a need, therefore, to integrate them into the model boundaries. Thus, besides the Mahury, measurements were also carried out in the Approurage and Oyapock rivers (Figure 2a) and estimated for the other smaller rivers using historical datasets. Wave data were collected by Phares et Balises from a buoy at a distance of 12 miles from the coast. However, no wave data are available for the study period because the buoy only began recording measurements in June 2016. Characteristics of waves were also extracted from the operational ocean wave predictions of NOAA/NWS/NCEP website (http://polar.ncep.noaa.gov/waves/ accessed on 29 September 2024) at the station 307.63° E; −5.98° N.

Bathymetric data were provided by the Cayenne Port Authority from measurements conducted at the estuary mouth and nearshore area (box in Figure 1b) using a Knudsen mono-beam and bi-frequency (33 and 210 kHz) echo sounder with 40 cm precision over consolidated bottoms. Where fluid mud was present, a plumb line was used to check the real depth due to the perturbations in the signal, especially for high frequencies. The definition of the bathymetry was based on a frequency of 210 kHz, which considers fluid mud with a density of 1.07. For the rest of the study area (Figure 2a), the data were provided by France's Service Hydrographique et Océanographique de la Marine (SHOM-MNT Guyane: https://diffusion.shom.fr/donnees/bathymerie/mnt-bathymetriques/mnt-facade-guyane-homonim.html accessed on 29 September 2024).

2.3. Satellite Data

Landsat 8 images were used to build and to validate the model. The Operational Land Imager (OLI) sensor has eight bands at 30 m spatial resolution and a panchromatic one at 15 m spatial resolution. OLI level 1 data (L1T) corresponding to the period between April 2015 and November 2015 were downloaded from the Earth Explorer database (https://earthexplorer.usgs.gov/ accessed on 29 September 2024). A total of 6 Landsat 8-OLI images (Table 1) were used after images highly affected by clouds were discarded.

Table 1. Dates of satellite images available during the six months of the model simulation and the corresponding forcing conditions.

Date	Tide (m)	Hs (m)	Flow Rate (m^3/s)	Wind Velocity (m/s)
29 July 2015	−1.08	1.23	91.36	6.41
30 August 2015	−1.61	1.25	47.08	7.60
15 September 2015	−2.01	0.73	33.38	4.99
1 October 2015	−2.41	0.95	23.20	6.30
2 November 2015	+2.87	1.15	12.74	5.46
18 November 2015	+2.79	1.31	22.53	3.85

Because of the characteristics of the OLI sensor, quasi-permanent glint contamination is present in the images selected. Thisresults in contaminated pixels, and to recover them, the images were corrected using the method proposed by [50]. Following the correction, ACOLITE software (acolite_win 20170718.0), developed at RBINS (Bruxelles, Belgium), was used to process L1T. SWIR processing was chosen, and a fixed epsilon computed on the data prior to sun glint correction was used. The methodology used is explained in [50], where a validation of the correction chain was performed for French Guiana.

SPM estimation was conducted using a semi-analytical algorithm developed by [51]. It covers four orders of magnitude, from clear to very turbid waters, and uses two distinct algorithms related to the turbidity of the water masses. The algorithm was developed for several sensors, including Landsat 8, and for several water masses, including those off French Guiana. The interested reader is referred to [51].

2.3.1. Coastline Extraction and Intertidal Areas

Landsat 8 2015 data were used to define the model coastline and intertidal areas for that year. Mudbank migration strongly impacts the French Guiana coastline, and due to the lack of up-to-date data in areas of the Oyapock and Approuage Rivers, Landsat 8 data were used. The physical environment of the intertidal zone of mud banks makes in situ surveying methods difficult to implement [30]. Landsat 8 data were therefore used for the extraction of the mudbank intertidal zone using the Normalized Difference Water Index (NDWI) [52]. The NDWI is based on a band ratio between the near-infrared (NIR) and visible green bands, but because of the high turbidity of the coastal waters of French Guiana, the SWIR2 band was used instead: $\mathrm{NDWI} = \frac{\mathrm{Green}-\mathrm{SWIR2}}{\mathrm{Green}+\mathrm{SWIR2}}$.

The depths corresponding to these zones were estimated using the tide height value and were referenced using the level "NGG77" for integration into the bathymetry.

2.3.2. Amazon Influence

SPM concentration values were used to characterize the Amazon influence in the coastal waters. SPM values were extracted from Landsat 8 2015 images and were linearly interpolated over time to the east boundary of the model.

2.4. Numerical Model Setup

The numerical model is built with the code Open TELEMAC based on finite element techniques and an unstructured mesh. Different modules are internally coupled in this setup: TELEMAC2D (T2D) for water circulation, SISYPHE for sediment transport, and

TOMAWAC (TWAC) for wave propagation. The different modules and datasets are described in the following sections. A 2D depth-averaged model has been selected as a preliminary approach to test the triple coupling with reasonable computational time. The code has been modified to include interactions between sediment transport and hydrodynamics. The proposed methodology focuses primarily on the interaction between mud deposits and wave propagation. The influence of fluid mud is accounted for by introducing an additional source term into the wave module, while the effect of mud concentration on the flow is considered through the bed friction coefficient. A 3D model should be used to further analyze sediment dynamics in the estuarine area, where saline stratification and sediment-density-induced effects [53] are stronger, particularly in the turbidity maximum zone, where high SPM concentrations are observed near the bottom.

2.4.1. Model Forcing Settings

In the coastal fringe, the tidal elevation and tidal currents were imposed via the recomposition of harmonics from TPXO Amazonian [54]. In the case of the upstream fluvial boundaries, eight rivers were considered. The discharge was measured upstream of the limit of tidal influence (about 100 km, [55]). However, especially during the rainy season, discharge at the mouth can be quite different due to water contributions from lateral streams near the coast and rain influence. The value for the Mahury estuary was corrected using the in situ data obtained at station DDC (Figure 2d) and considering the watershed area of 3650 km^2 [56].

Wind data were downloaded from the European Centre for Medium-Range Weather Forecast (ECMWF) ERA-Interim global atmospheric reanalysis (10 m windgrid resolution 0.125 × 0.125 and data every 6 h). Time series of waves from the numerical model Wave Watch III were imposed on the offshore boundary. Three-hourly time parameters of wave characteristics (significant height of combined wind waves and swell (m); primary wave mean period (in s); and primary wave direction (in 0 deg from north and 90 deg from east)) were linearly interpolated at intervals of the model boundaries.

2.4.2. Model Domain

The selected simulation domain extends from the National Park of Cape Orange (North Brazil) to the Kourou River estuary area (French Guiana), over a total length of 258.6 km and a cross-shoredistance of 74.8 km (Figure 2). All eight rivers were considered for the modelling purpose, in addition to the Mahury, Approuague and Oyapock that directly affect the study area (Figure 2). The unstructured mesh is composed of 28,430 nodes, with a progressive refinement from the maritime area to the estuary. The density of the mesh is higher around the islands in front of the Mahury estuary (between 50 and 100 m) and in the area closest to the estuary (between 150 and 650 m) (Figure 2b,d) than in the rest of the coastal domain (2.5 km), to better represent the hydrodynamic forcing in the former area. The distance between the nodes inside the rivers varies from 25 m (lowest value) for the Mahury River to 2.5 km (highest value) offshore.

2.4.3. Hydrodynamic Model—TELEMAC2D

Shallow water equations were solved with T2D. The friction equation of [57] was integrated in order to take into account the drying and wetting of intertidal flats. The bed shear stress was then computed as follows:

$$\tau_b/\rho = u_*^2 = f_A u_{*turb}^2 + u_{*lam}^2 = f_A\left[\frac{\kappa U}{\ln\left(h/z_0\right) - 1 + z_0/h}\right]^2 + \left[\sqrt{\left(\frac{3}{2}(z_0 + \beta\varphi h)\frac{U}{h}\right)^2 + 3\frac{U}{h}\nu(\varphi)} + \frac{3}{2}(z_0 + \beta\varphi h)\frac{U}{h}\right]^2$$

where τ_b isbed shear stress (kg m^{-1} s^{-2}); ρ is thethe density of water (kg/m^3); u_* is theshear velocity (m/s); u_{*turb} is theshear velocity for fully developed turbulent open-channel flow (m/s); u_{*lam} is theshear velocity for laminar open-channel flow (m/s); κ is von Karman

coefficient (which decreases from the clear water value 0.41 to lower values depending on the sediment load); U is the local depth-averaged flow velocity (m/s); h is the local water depth (m); β is the suspension friction (or apparent roughness) coefficient, which is 0.045; ν_w is water viscosity (m^2/s); φ is the volumetric suspended particle concentration; and z_0 is the effective roughness length scale (m). For further details on how bed roughness was integrated into the model, the reader is referred to [57].

As model initialization, a spin-up simulation was performed (from 1 January to 30 April) with constant flow rate values. The initialization run serves to start the sediment transport with an initialized hydrodynamic field.

2.4.4. Sediment Model—SISHYPE

Suspended sediment transport and bed changes were computed using SISYPHE [58]. Erosion and deposition were computed by applying the classical Krone–Partheniades laws [59]. The relationship between critical shear stress τ_{ce} and the mud concentration C layer was calculated according to [60]:

$$\tau_{ce,layer} = 0.024 \times e^{0.0103 * C_{layer}}$$

The influences of both waves and currents on the bed shear stress are included. Settling velocity is based on Figure 7 of [61]. As pointed out by [62], consolidation processes in the Mahury are slower than in other estuarine configurations. As, in the present study, the time period considered is short (1 to 6 months), consolidation processes are not explicitly considered here to also reduce the number of calibration parameters. They are, however, implicitly included by imposing different bed structures for both seasons. The two initial bed structures are defined using in situ data from [29] (see Figures 7–9 in [29]) and integrated into the model for the rainy and dry seasons according to the observations. These data were collected close to the mouth of the Mahury (up to 10 km offshore and 20 km alongshore) and do not cover the whole numerical domain. During the dry season, only the navigation channel exhibited significant fluid–mud layers, with a more heterogeneous surface density spatial distribution. However, the leading and trailing edges of the mud bank were still characterized by fluid and consolidated mud (>1400 kg/m^3, depth between 4 and 5 m).The inner part of the mud bank displayed higher densities (1250–1400 kg/m^3) than during the rainy season due to self-weight consolidation processes. For the rainy season, a thick (>1.5 m) fluid mud layer (1100 and 1250 kg/m^3) was present at the entrance of the estuary in the navigation channel (Figure 1b). The trailing edge, near the shoreline, was also characterized by another important fluid mud layer. Therefore, when evaluating the influence of the various dynamic situations for the rainy season, the bed layers and mud location were based on a consideration of the rainy season measurements, whereas for the dry season, the bed layers and mud location were modified in the model to consider the effects of consolidation observed in the measurements.

As explained above, even though consolidation is not considered in the model, the difference identified between the rainy and the dry season due to this process [29] is integrated into the model by modifying the mud density location and the mud layers (as on Figures 7–9 in [29]). Nine bed layers were considered in the model using the measurements from [29], and the first four had a density of less than 150 kg/m^3.

The configuration under study corresponds to a period when a mud bank is present near the mouth, with mud dominating the bed composition. However, during the inter-bank period, which is not analyzed here, sand banks can be observed near the mouth. A combined sand–mud approach should be used to analyze sand bank migration, particularly during storms [63].

2.4.5. Wave Model—TOMAWAC

The third-generation wave model TOMAWAC (TWAC) was used to transform wave conditions from offshore to inshore and to integrate the effect of wave–mud interaction. The internal coupling between T2D and TWAC allows us to account for the effect of

the waves on the mean circulation (e.g., wave-induced currents that lead to longshore transport), as well as on the modulation of waves by tides. The dissipation mechanisms considered were white-capping dissipation, based on the formula of [64], bottom friction dissipation, with a bottom friction coefficient of 0.038 m^2/s^2, depth-induced breaking dissipation following the formulation of [65], and non-linear transfers between frequencies in accordance with the formula of WAM cycle 4 (DIA method). The effect of wave–mud interaction is also considered. In the case of muddy bottoms, the pressure variations caused by wind-generated surface waves can result in motion of the water/seabed interface. This motion, and particularly in the case of muddy bottoms, is damped by viscosity. There are different methods for estimating the damping of water waves by viscous mud. In this study, the following formulation developed in [38] was integrated into the model as an addition to the action balance equation through the total of source/sink terms expressed as wave energy density:

$$S_{mud} = -2C_{g,mud}k_i$$

where k_i is the imagery part of k_{mud} and $C_{g,mud}$ is the mud modified wave group velocity; it operates by solving a modified dispersion relation, where the wave number being solved for k_{mud} is a complex number computed as follows:

$$k_i \approx D_{mud} \equiv \frac{\delta_m (B_r' + B_1')k_1^2}{\sinh 2k_1 h + 2k_1 h}$$

where δ_m is the Stokes boundary layer thickness for mud, h is water depth, k_1 is the leading order of the real part of the mud-modified wave number k_{mud}, respectively, in a Taylor expansion about the mud–water interface, and D_{mud} is the leading order term in the full expansion of ki. B_r' and B_1' are, respectively, the real and imaginary parts of B and their expressions are given in Appendix A of [38].

The formulation of [38] is a simplification of the [39] formula, but it produces very similar results for the range of mud characteristics used by [36]. As indicated by [36], very rapid wave attenuation depends on mud characteristics and water depth. Viscosity was considered 10^{-3} m^2/s for mud presenting a concentration lower than the 150 kg/m^3 following the results obtained by [21] on the Guyana coast. The effect of mud on the waves was taken into consideration for those areas with a mud depth exceeding 0.2 m.

2.4.6. Model Run

Numerical model calibration and validation were performed by comparing in situ measurements on water level, flow velocity, and SPM, with satellite-derived measurements for SPM values and spatial patterns. A six-month simulation (starting May 2015) was used to validate the model and the sediment input parameters. These were kept for the running of the model, adjusting only the fluid mud location and thickness according to the measurements by [29] (see Section 4.4). Afterwards, one-month simulations were carried out for the rainy (June) and the dry season (19 September–20 October) of 2015 to assess the impact of waves and tides over sediment fluxes, considering (a) no waves, (b) waves without wave–mud interaction, and (c) wave–mud interaction using the [38] model. All the simulations covered different tidal ranges, neap to spring, and wind and wave conditions.

The sediment rate transport was computed to assess the impact of the different forcing dynamics over the mud bank, as follows:

$$Q\left(kg \cdot \frac{s}{m}\right) = U\left(\frac{m}{s}\right) \cdot h(m) \cdot C\left(\frac{kg}{m^3}\right) \quad (1)$$

where U is the velocity, h is the water depth, and C is the suspended load concentration.

3. Results

3.1. SPM Patterns

As a preamble, before presenting the SPM patterns, it is important to note that the model satisfactorily replicated the water level for the DDC-Tide station (RMSE = 0.15) (Figure 3a). The flow velocity prediction was good for the DDC station (RMSE = 0.16) and for S2 (RMSE = 0.15) (Figure 3b).

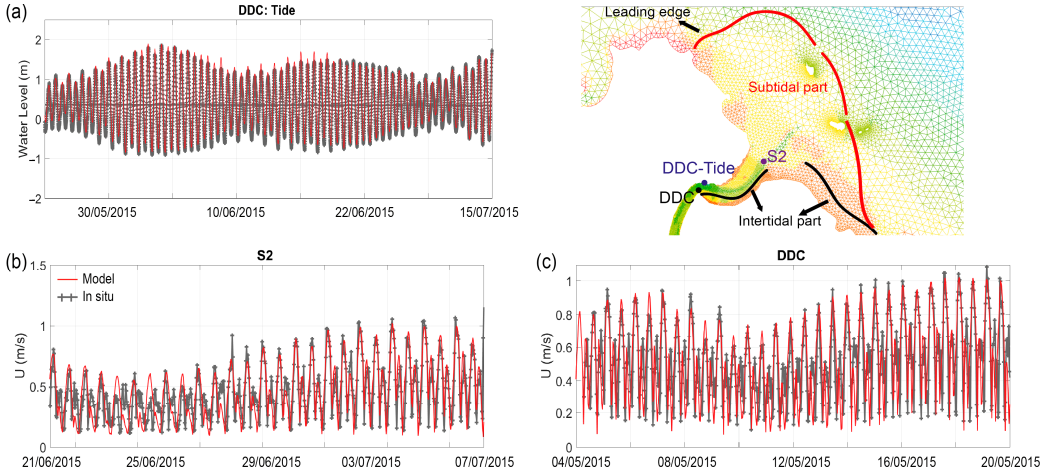

Figure 3. Model output (red) and water levels and flows (grey) at DDC-tide, DDC, and S2. (**a**) Water level observations at DDC-tide; (**b**) velocity model output compared to S2 observationsand (**c**) to DDC observations. Locations of stations are shown in the top-right panel.

Regarding the modelled SPM spatial patterns, these were compared to those obtained using remote sensing and in situ data (Figure 4). The model correctly reproduced the observed SPM peaks for station S2 (RMSE = 0.26) (Figure 4a), even though concentration values differed from those observed. Due to biofouling, in situ SPM results after 29 June 2015, were discarded. The comparison was carried out after normalization of the modelled SPM outputs and satellite SPM data based on the concentration value of the 95thpercentile. This normalization is a prerequisite for comparison, as satellite data are obtained at the water surface, whereas the model provides averaged SPM values in the water column. The intertidal part presents normalized SPM concentrations of ~0.91 and ~0.93 for the model- and satellite-derived SPM, respectively (Figure 4c,d). The model also correctly reproduced the concentration at the back of the bank (Figure 4c), with an RMSE value of 0.06 (Figure 4e). Over the subtidal part, the observed normalized SPM values were between 0.49 and 0.9 for the satellite-derived data (Figure 4c) and between 0.52 and 0.91 (Figure 4d) for the modelled SPM. However, high RMSE values are observed at the leading edge of the mud bank and in the offshore area at the back of the bank (Figure 4e). The plume from the satellite image seems less diffuse than the modelled one. Even though the plume extension is more diffuse in the model, the highest normalized SPM values (~0.91) have an alongshore extension similar to that of satellite-derived data (Figure 4c,d).

3.2. Hydrodynamic Forcing

This section analyses the influence of forcing on SPM and sediment transport patterns, as SPM can be considered a proxy for the location of mud banks [18,66]. Wind waves and tidal currents have been considered fundamental in the erosion and deposition processes affecting mud banks [33]. Therefore, the analysis focuses on SPM and sediment transport variations due to (1) waves during a neap cycle and (2) tidal variations (neap–spring).

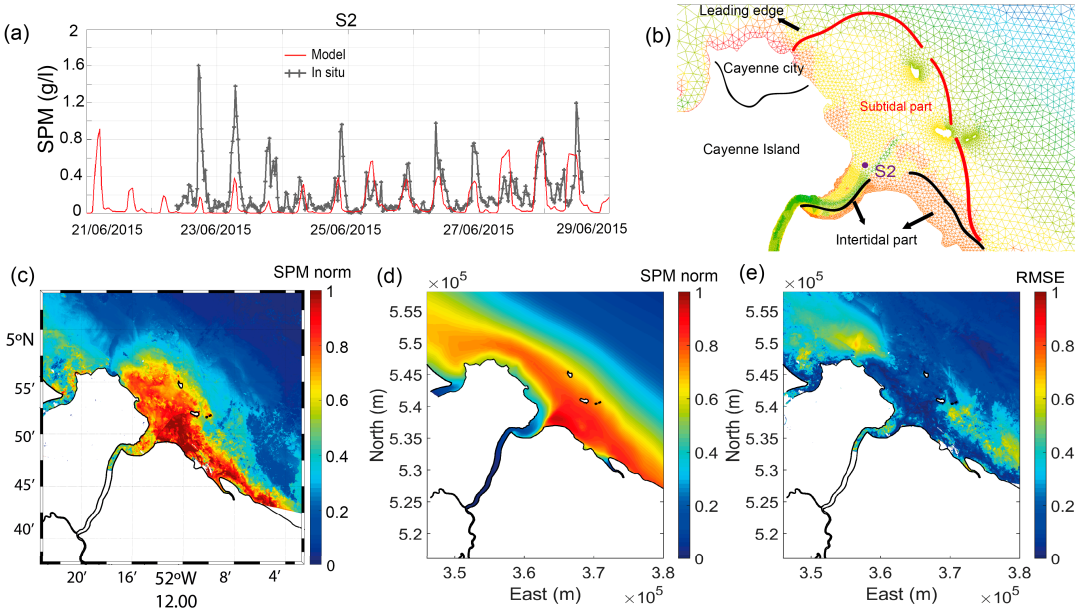

Figure 4. Validation of SPM values. (**a**) Modelled SPM compared to S2 in situ measurements, (**b**) location of station S2, (**c**) averaged and normalized satellite SPM data for the six-month validation period, (**d**) averaged and normalized SPM concentration values for the six-month validation simulation, (**e**) RMSE values estimated comparing modelled SPM outputs with satellite-derived SPM.

3.2.1. Wave Influence

The averaged wave height outputs were estimated for the rainy and dry season simulations based on the Ng model (Figure 5). The influence of fluid mud thickness on wave heights can be noticed in the nearshore area. During the rainy season, the intertidal area shows average wave heights between 0 and 0.31 m (Figure 5a). Wave heights are slightly higher in the leading edge of the mud bank where they attain up to 0.34 m. During the dry season, fluid mud is mainly located in the navigation channel, and waves in this area reach minimum heights of 0.28 m (Figure 5b).

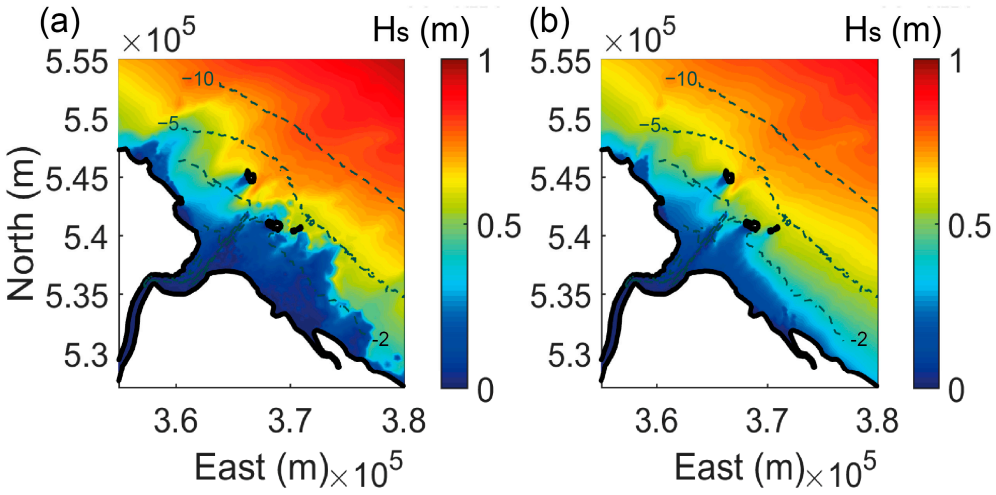

Figure 5. Averaged model wave height outputs for the (**a**) rainy and the (**b**) dry season.

In 2015, due to technical issues with the buoy, no wave measurements were available. TWAC outputs were validated against in situ measurements from 2016 made outside the mud bank extension area. The model effectively captures the peak period. For H_{m0}, although peak heights are underestimated, the overall trend is well represented (RMSE 0.26. To date, no measurements are available near the shore. Additional surveys are needed to further validate wave propagation.

Rainy Season

The SPM patterns and associated sediment fluxes (Equation(1)) estimated for different wave conditions during one neaptide cycle are shown in Figure 6. Three scenarios were considered: (1) only circulation generated by tidal and wind-generated currents (Figure 6a,b), (2) waves and circulation (Figure 6c,d), and (3) waves and circulation including wave damping via the Ng approach (Figure 6e,f). The selected neaptide cycle was characterized by a mean wave height of ~1 m and a peak period of ~7.6 s (see Figure 1d) offshore of the mud bank (ca. 20 km from the shore). A neap cycle was selected because mud mobilization mainly occurs after periods of low wave forcing at the end of the dry season and during neap tides [16,20].

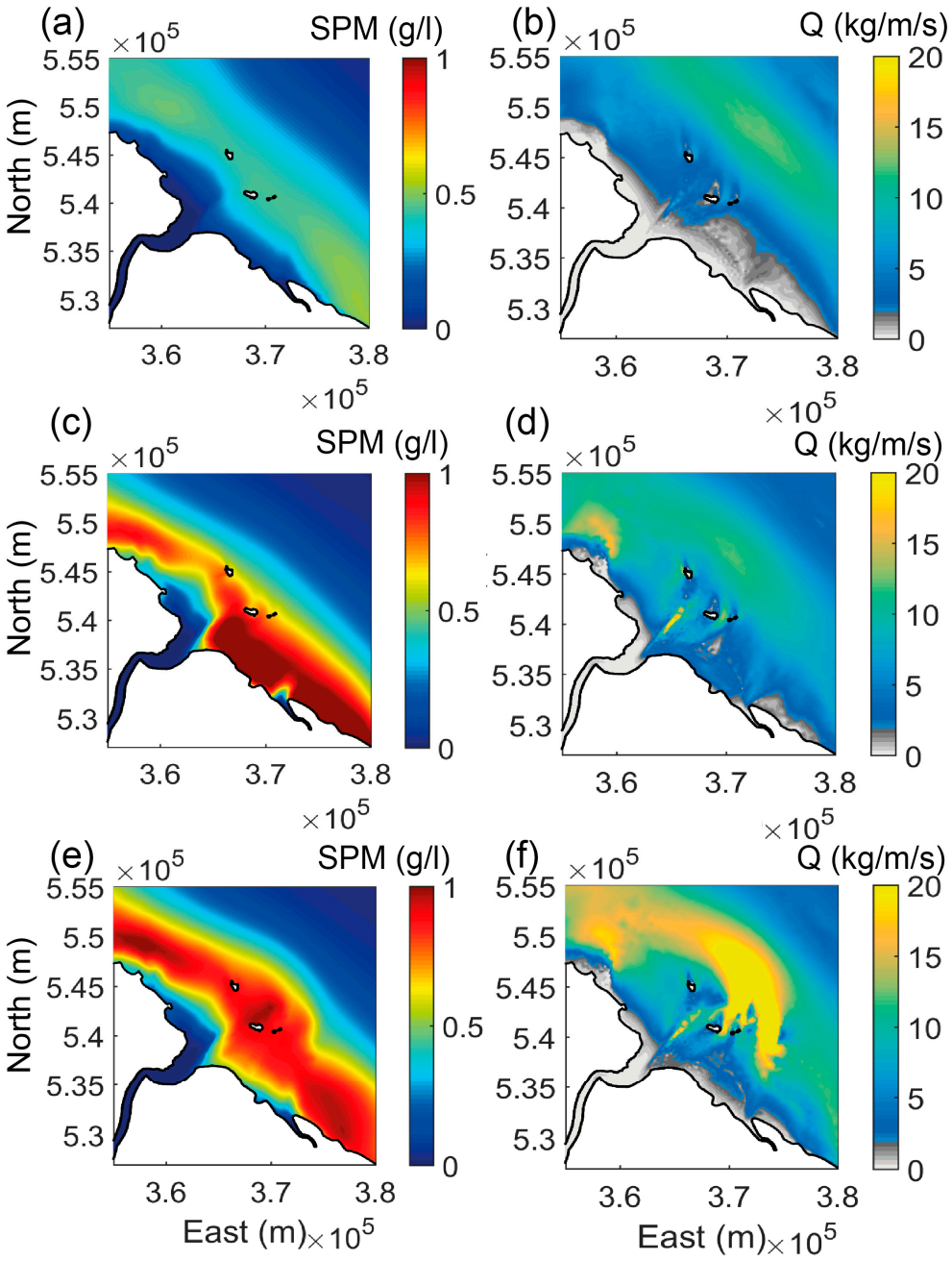

Figure 6. SPM and sediment transport outputs for different conditions during the rainy season. (**a**) SPM and (**b**) transport with tides and wind-generated currents, (**c**) SPM and (**d**) transport, also including waves, (**e**) SPM and (**f**) transport using the Ng formulation for the wave–mud interaction.

In the first scenario, the influence of the rivers on SPM is clearly visible for the area close to the mouth of the estuary (Figure 6a). Moreover, sediment transport is considered insignificant (<5 kg/m/s) in this area. However, the rates in the near-offshore coastal area oscillate between 9.8 and 17.6 kg/m/s due to the influence of tides and currents (Figure 6b).

For the second scenario, SPM concentrations over the intertidal part of the mud bank reach a maximum of 1.23 g/L (Figure 6c). An SPM plume is observed parallel to the coastline with lower SPM values than the wave–mud interaction simulation (Figure 6c,e). As observed by previous studies [33,66], when wave–fluid mud interactions are lacking, resuspension tends to reduce SPM concentration. The influence of the Mahury estuary creates a low SPM-concentration 'belt' in the nearshore area of Cayenne (Figure 6c). However, sediment transport displays maximum rates at the navigation channel (19.1 kg/m/s) and in the area northwestward of Cayenne (Figure 6d). The intertidal part shows transport rates that are considered insignificant (<4.5 kg/m/s) (Figure 6f).

With wave–mud interaction, a more developed SPM plume is observed over the subtidal area (Figure 6e) and is delimited by the −5 m contour (Figure 1b). This depth has been considered a limit for wave action and remobilization in previous studies [18,21,29]. The outer mud bank at the trailing edge is characterized by SPM values close to 1 g/L due to wave resuspension. However, the intertidal part shows concentrations that are lower than in the second scenario. In the subtidal part, and between the coastline and the −5 m contour, sediment transport rates are much lower (9.6 kg/m/s). The navigation channel shows high rates of sediment transport (up to 18.5 kg/m/s).

Dry Season

The same scenarios wereconsidered for the neaptide cycle in the dry season: tidal and wind-generated currents (Figure 7a,b), but also wave-generated currents (Figure 7c,d) and the addition of wave–mud interaction (Figure 7e,f). During the dry season, fluid mud is mainly located inside the navigation channel and the inner mud bank is characterized by an increase in mud density compared to the rainy season ([29]; Figures 8 and 9 on the paper). These patterns were integrated into the model as explained in Section 2.4.4.

As no important differences are observed among the three simulations in the coastal area, the sediment flux is mainly controlled by circulation (Figure 7). However, compared to the rainy season, changing spatial patterns for SPM and sediment transport are now located inside the mouth of the Mahury estuary (Figure 7).

The highest SPM concentrations occur in the first 4 km of the nearshore area (Figure 7a,c,e). Concentrations are four times lower than during the rainy season, which is in agreement with a previous study [66], and SPM is constrained between the coastline and the 2 m depth contour. For the first scenario simulation (Figure 7a), SPM concentration shows maximum values at the outer part of the back of the bank and the leading edge of the intertidal part (>0.24 mg/L).

In contrast, the estuary mouth and the intertidal area exhibit stronger SPM values when wave-generated currents are added (Figure 7c,e). The influence of wave–mud interaction is clear in the third simulation scenario (Figure 7e), as SPM concentrations increase in the very nearshore area and the estuary mouth, proving the influence of wave–mud interaction in SPM resuspension and, thus, erosion.

The dry season is characterized by low sediment transport in the subtidal (~3.87 kg/m/s) and intertidal (<0.7 kg/m/s) parts of the mud bank when compared to the offshore area (Figure 7b,d,f). The density of the mud increases in the inner sector of the subtidal part of the bank during periods of low wave energy [29]. The main difference between the three simulations occurs in the mouth of the estuary (Figure 7b,d,f), where sediment transport rates are affected by waves, leading to increased values on both estuary flanks and up to 9.4 km upstream from the mouth (Figure 7d,f).

The model setup, including the wave–mud interaction, is kept for the analysis of the tidal influence.

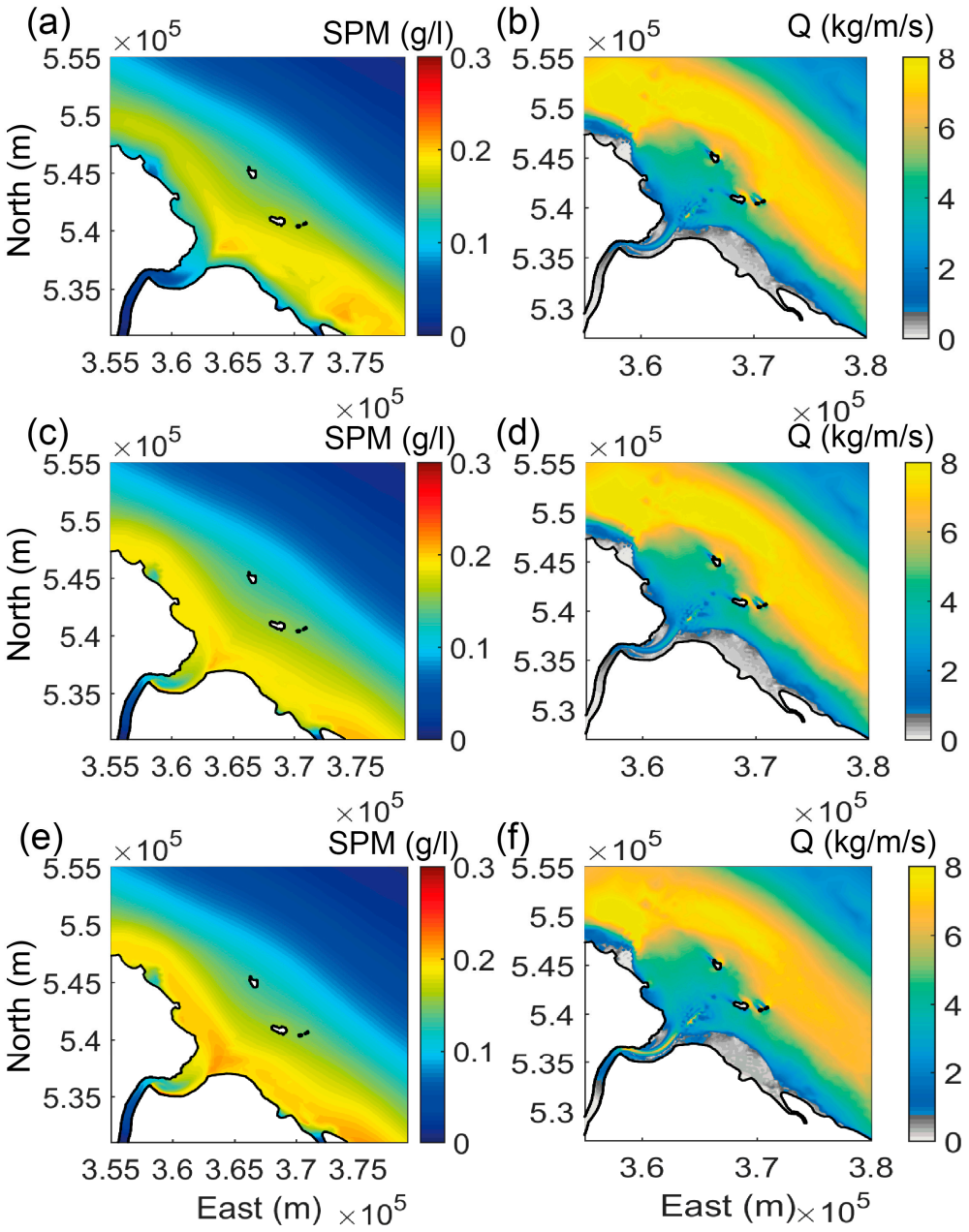

Figure 7. SPM and sediment transport outputs for different conditions during the dry season. (**a**) SPM and (**b**) transport with tides and wind-generated currents, (**c**) SPM and (**d**) transport, including wave currents, (**e**) SPM and (**f**) transport using the Ng formulation for the wave–mud interaction.

3.2.2. Tidal Influence

Neap–spring cycles under similar climatic conditions were analyzed for the rainy and the dry season (Figure 8). Wave height values oscillate between 0.95 and 1.08 m (at a depth of 20 m) in both seasons, whereas wind speed shows values between 5 and 6 m/s for the dry season and 3.4 and 5.1 m/s for the rainy season. Therefore, the neap and spring cycles in each season could be compared, with differences in between seasons being related to wind, fluid mud location, and flow rate.

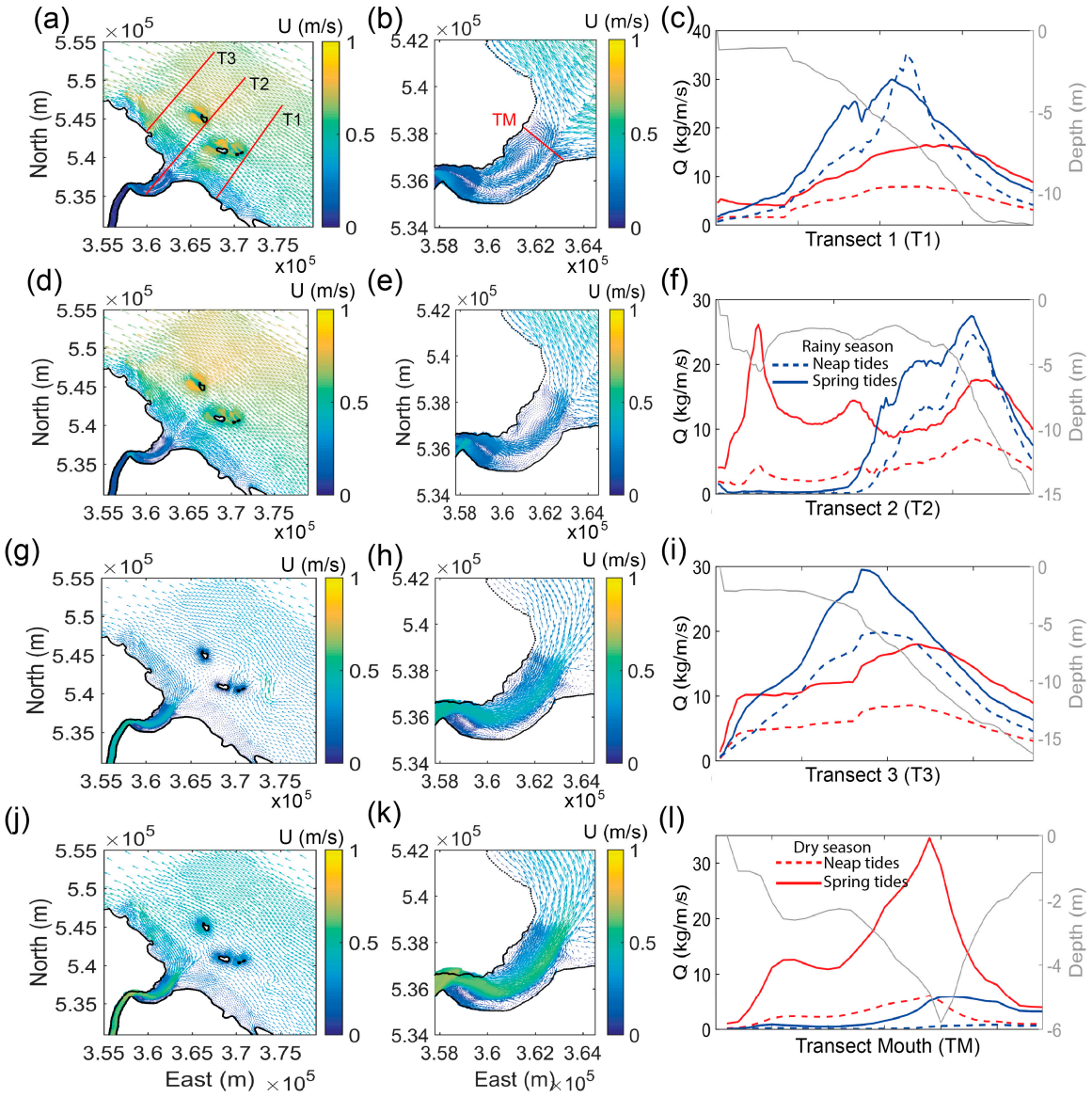

Figure 8. Tidal influence on flow velocity and sediment transport over four different transects (**a**,**b**). (**a**) Average flow velocity for a neaptide cycle during the dry season and (**b**) zoom in on the Mahury estuary mouth. (**d**) Average flow velocity for a springtide cycle during the dry season and (**e**) zoom in on the estuary mouth. (**g**) Mean flow velocity for a neaptide cycle during the rainy season and (**h**) zoom in on the estuary mouth. (**j**) Mean flow velocity for a springtide cycle during the rainy season and (**k**) zoom in on the Mahury estuary mouth. (**c**) Transport values ofprofile T1 for the dry (red lines) and the rainy season (blue lines) and for the neap (dashed lines) and spring tides (continuous lines). Transport values for (**f**) profile T2, (**i**) profile T3, and (**l**) profile TM for the dry and the rainy season and for the neap and spring tides.

The mean flow velocity is parallel to the coastline; thus, it is alongshore and generally follows the isobaths (Figure 8b,e). Nevertheless, during the rainy season and especially during the neap tide, a narrow and strong north-northwestward current appears at the east side of the islands, probably generated by the presence of fluid mud east of La Mère islet (Figure 8h,k). Cross-shore velocities vary from a minimum of 0.05 m/s in the intertidal area for the neap cycle of the rainy season to a maximum of 0.65 m/s offshore for the spring cycle of the dry season (Figure 8), values in agreement with those of the previous numerical study of [33].

Flow velocities along the coast vary between both seasons and tidal cycles. In the coastal area, spring tide velocities are stronger for both seasons and the dry season is characterized by the strongest values (Figure 8b,h,e,k). However, the mouth of the estuary shows the opposite tendency. Here, because of river discharge, the strongest values occur during the rainy season (Figure 8c,f,i,l). The high river discharge leads to stronger seaward-oriented currents during the spring tidal cycle. However, the dry season is characterized by landward-oriented currents along both flanks of the estuary mouth but by seaward-oriented currents in the channel. It is noteworthy that velocities decrease in the coastal part of the navigation channel during both seasons (Figure 8b,e,h,k).

To evaluate the influence of tidal currents on sediment transport, four different transects were set up. Three of them are perpendicular to the coast and located in the back of the bank (T1), in the channel of the estuary (T2), and in the leading edge of the mud bank (T3). The fourth transect runs across the mouth of the estuary, from west to east (TM) (Figure 8a,d,g,j). Mud remobilization is noticeable during spring tides for both seasons, especially in the mouth of the estuary. Nevertheless, during the neap cycle of the rainy season, a peak of sediment transport is observed around the −6 m isobath at the back of the bank due to the narrow flow path of the strong north-northwestward current. The ~−6 m isobath marks the appearance of maximum transport peaks for all tidal conditions during both seasons (Figure 8a,d,g), with a maximum of 36.5 kg/m during the rainy season. As highlighted earlier, the −5 m isobath was considered the limit of wave action and SPM remobilization; thus, high sediment transport rates are expected around this depth. The outer part of the back of the mud bank is the most active part of these banks [29,67], as the highest transport rates occurred between the −2.5 m and −7 m isobaths (Figure 8a; T1). In the front of the bank (Figure 8g; T3), sediment transport is quite constant up to a depth of 3.8 m, showing the impact of fluid mud, as during this season, the latter is mainly located around the −6 m isobath. The fluid mud layer over the subtidal part of the mud bank is thicker during the rainy season [29].

Inside the estuary, transport rates are 3.9 times lower than those in the coastal area, with the exception of spring tides during the dry season, which show values comparable to those of the rainy season in the coastal area (Figure 8j). Moreover, the observed patterns differ from those in the coastal zone (Figure 8d,j). The highest transport rates are obtained during the dry season between the west flank and the channel. In addition, spring tides, compared to neap tides, exhibit the strongest transport rates (Figure 8d,j), as observed in [28].

3.2.3. Preliminary Insights into Daily (Ebb–Flood) Circulation and Sediment Transport Patterns

To explore the potential accumulation areas, erosion–sedimentation patterns during an ebb–flood cycle wereanalyzed according to the evolution of the first two fluid bed layers (see Section 2.4.4) (Figure 9). During neap tides for the rainy season, net sediment transport follows the −5 m isobath and is mainly driven by ebb tides at the back of the bank (Figure 9a). However, in the inner part of the mud bank and in the intertidal area, net transport is mainly driven by flood tides, with a net west-southwest direction towards the coast (Figure 9a). This would contribute to the appearance of a potential accumulation zone at the leading edge of the intertidal area. This part is composed of fluid to soft mud (<650 g/L; [68]) and is formed by the accumulation of mud due to wave damping [69], observed at the back of the bank along the −2 m isobath. The leading edge of the subtidal zone also presents a potential accumulation area, in agreement with previous observations of mud accumulation in this zone coming from the back of the bank [29,67]. Also, given the net transport patterns observed, mudbank migration could be enhanced by ebb currents, which tend to be stronger in the area [28]. Nevertheless, flood currents could enhance net sediment transport in the inner part of the mud banks.

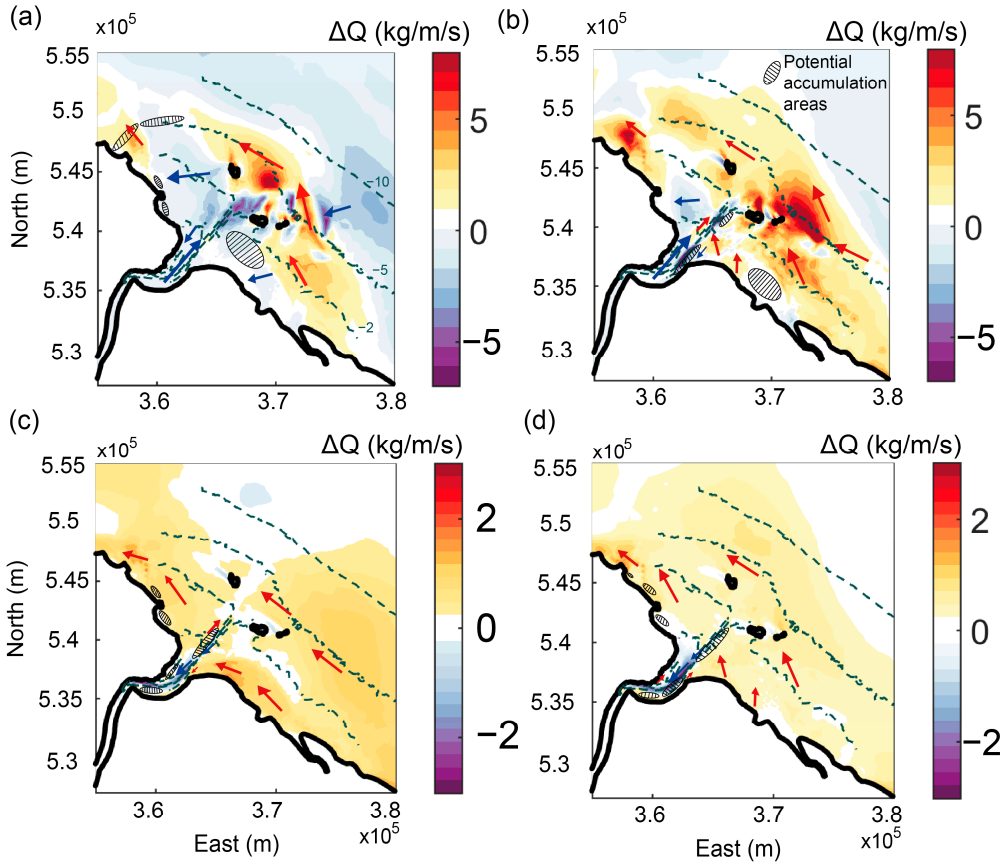

Figure 9. Sediment transport at daily cycles as a difference between the ebb and the flood tide. (**a**) Sediment transport for a neap and (**b**) a spring cycle during the rainy seasonand (**c**) for a neap and (**d**) a spring cycle during the dry season. Reddish colours correspond to areas where ebb sediment transport presented higher values than flood sediment transport. On the contrary, areas with higher flood sediment transport are characterized by bluish colours. Red arrows represent the direction of sediment transport in those areas dominated by ebb tides and blue arrows correspond to those dominated by flood transport. Black hatched ovals represent accumulation areas between ebb and flood.

During spring tides in the rainy season, net sediment transport is mainly driven by ebb tides (Figure 9b). In contrast, the mouth of the estuary and the western side of the subtidal part close to the estuary, including the navigation channel, show a flood-driven net transport. Three potential accumulation areas have been found under these conditions (Figure 9b), one of them being the trailing edge of the intertidal area in agreement with a previous study [69], since sedimentation occurson the consolidated mudflat at high tide during spring tides. The east flank of the estuary mouth also presents a potential accumulation area due to the influence of landward-directed flood transport (Figure 9b).

Net sediment transport is mainly influenced by ebb tides in the coastal area during the dry season. Nevertheless, the estuarine part of the navigation channel is mostly affected by flood tides (Figure 9c,d). During neap tides, sedimentation in the coastal area of the navigation channel and the estuary mouth is considerable, as three potential accumulation areas occur (Figure 9c). During periods of low wave energy, as during the dry season, rapid shoreline advance is favoured by self-weight consolidation [29], which could explain the accumulation of sediment inside the estuary (Figure 9c). During these wave conditions, the thickness of the fluidmud layers in the navigation channel is maintained [29], as confirmed by the presence of a potential accumulation area (Figure 9c). Moreover, two accumulation areas appear in the very nearshore area in front of Cayenne, again under neap

tide conditions during the dry season (Figure 9c). These accumulation areas are regularly visible at low tide since they often take the form of bar-like features [70].

During spring tides, net sediment transport rates are almost constant over the entire study area, contrary to the patterns observed during neap tides, where stronger values are observed in the nearshore sector of the leading edge of the intertidal part. The navigation channel presents a landward flood-driven net transport and is potentially an important accumulation area, coincident with the location of fluid mud (Figure 9d). However, at both flanks of the estuary, the net transport is seaward and ebb-driven (Figure 9d).

For both seasons, the river discharge is mainly concentrated in a narrow jet in the deep channel. The ensuing velocity gradients could enhance the appearance of potential accumulation areas, as observed in Figure 9. Net sediment transport is lower during the dry than the rainy season (Figure 9).

4. Discussion

Numerical studies focussing on the nearshore dynamics along the muddy coastline of the Guianas have generally either considered the coastline without taking into account the estuarine influence or wave propagation without mud dynamics. To investigate the main forcings involved in sediment exchanges between the Mahury estuary and an Amazon-derived coastal mud bank in French Guiana, a 2D numerical model was built with dynamically coupled modules of the circulation, waves, and sediment transport to integrate mud effect on wave damping. Given the complexity of the area and the myriad processes involved, this approach provides a foundational basis for further development and refinement of more comprehensive models that could more accurately represent the full range of dynamics.

The accuracy of the model has been assessed with different available datasets. Several numerical simulations were conducted to examine the seasonal variation in SPM according to different forcing dynamics. These simulations offer preliminary insights into the dynamic interactions and sediment balance of the coast and an estuarine system. Estuaries are generally considered as net sediment sinks sourced commonly by riverine sediment flux but also in many cases by alongshore-derived sediment. The overwhelming influence of mud banks migrating along the Guianas coast from the mouths of the Amazon has implied that this alongshore source dominates in the Mahury, and various other estuaries, lying on this coast. However, the sediment transport and mud accumulation processes in this seasonal, equatorial tropical setting are complex and strongly spatially modulated (cross-shore and alongshore) by seasonal variations in wave energy and river discharge that are further expressed in the course of the neap–spring tidal cycle.

Our preliminary results show, first and foremost, high SPM concentrations in the nearshore area compared to those 20 km offshore [71], thus highlighting the importance of mud dynamics in the sometimes rapid shoreline changes that have been consistently identified on this coast (see, e.g., [16,20]). This leads, in turn, to wave height attenuation as a result of an increase in fluidmud thickness as observed by [29]. The influence of wave–mud interaction becomes evident in the third simulation scenario, as SPM concentrations increase in the very nearshore coastal area and the estuary mouth. This highlights the role of these interactions in SPM resuspension and associated erosion processes. As observed by previous studies [33,66], however, when wave–fluid mud interactions are lacking, resuspension tends to reduce SPM concentration.

The subtidal plume associated with the mud bank fluctuates with the tide and with the wind-generated longshore current. The fact that the plume from the satellite image seems less diffuse than the modelled one may be attributed to limitations in the model's representation of the mud bed beyond the in situ data coverage or the influence of unaccounted sandy sediments. The density of the mud increases in the inner part of the subtidal part of the mud bank during periods of weak wave energy [29], and observations suggest that this could be potentially related to the low sediment transport in this area. The fluid mud layer over this subtidal part of the mud bank is thicker during the rainy season [29]

due to wave remobilization [20]. In the dry season, as wind and waves are less strong and fluid mud thickness diminishes due to consolidation processes, a lower sediment transport ensues. The leading edge of the subtidal zone appears to function as a potential accumulation area, in agreement with previous observations of mud accumulation in this zone following remobilization from the back of the bank [29,67], as further discussed below. Further inshore, wave–mud interaction generates wave refraction zones that lead to an increase in SPM, especially at the back of the mud bank. The outer part of the mud bank in this trailing edge is characterized by SPM values close to 1 g/L due to wave resuspension.

The preliminary results of the 2D model highlight that wave damping is very important in the rainy season. Sediment transport during this season occurs along the −5 m isobath and from the trailing to the leading edge of the bank. The back of the mud bank is not protected by soft mud and is thus is eroded by wave action combined with a minor influence of tidal and wind-induced geostrophic currents [72]. This pattern thus corresponds to preferential mud transport by the constant action of waves during the rainy season, especially during neap tides, from the trailing to the leading edge, which results in the migration of the mud bank [26,67]. The model captures these migration patterns effectively, from the trailing to the leading edge. This migration process leads to mud accumulation at the leading edge of the mud bank, enhanced by ebb currents, which tend to be stronger in this area [28]. The intertidal part exhibits transport rates that are insignificant and tends to be characterized by sedimentation during this season and during high tide at spring tide, a process favoured by this mud mobilization and migration process. As no important differences are observed between the three simulations in the coastal area, the sediment flux seems to be mainly controlled by this circulation. The normalized SPM concentrations of ~0.91 (model) and ~0.93 (satellite-derived) for the intertidal part show the pertinence of the model results. The observed spatially patchy SPM distribution pattern is identical to that classically identified over mud bank areas [18,66,71,73].

Within this general spatial–temporal frame, the presence of the Mahury estuary plays an important role in the sediment dynamics. During the rainy season, the strength of the river flow limits mud deposition in the navigation channel and at the mouth. This mud deposition occurs on the neighbouring sandy beaches flanking parts of the estuary and at the front edge of the bank. During the dry season, fluid mud is mainly located in the navigation channel of the estuary and the mouth, under conditions of low river discharge, and the circulation is highly impacted by waves during this season, leading to the modification of sediment transport patterns inside the estuary, a general increase in SPM values, and detected accumulation patterns. The navigation channel during this season thus displays maximum transport (mud mobilization) rates. Sedimentation mainly occurs within the estuary and the nearshore area and appears to be mainly ebb-driven (more wave dissipation), leading to rapid shoreline accretion on both estuary flanks, but especially on the leeward-located (relative to wave incidence) east bank of the estuary during neap tides. The potential accumulation east of the navigation channel could result from the impact of high river flow on the current and wave field. River discharge probably hampers the coastal current, in a way similar to a hydraulic groyne effect [26,29], thus favouring sedimentation. This sedimentation seems to lead to an increase in the intertidal areas inside the estuary. The turbid pattern not detected by the 2D model that is observed at the estuary mouth may be due either to the fact that stratification is not considered here or to the description of the bed structure. It must be noted that mud thickness and density measurements [29] were carried out only at the outer part of the mouth of the estuary; thus, resuspension in this area could be impacted as mud thickness values were interpolated for the rest of the mouth.

The high mud concentrations within the navigation channel of the Mahury estuary [29] also have serious implications for both the management of the commercial port of Degrad des Cannes and for beach dynamics downdrift in the Cayenne area [74,75]. This high mud concentration in the channel necessitates constant dredging during this season, but it also creates a low SPM concentration 'belt' in the nearshore area east of Cayenne, westward of

which the mud transport rate increases once again. However, flood currents can enhance net sediment transport in the inner part of mud banks, and this could be the main factor responsible for the presence of two potential accumulation areas in the very nearshore area in front of Cayenne (Figure 9a). Ref. [29] suggested 'en masse' fluid mud transport nearshore and in the leading edge during periods of frequent high waves, which, as observed in Figure 9a, could be intensified by flood currents during neap tides. The high mud concentrations in the Cayenne area can lead to the embayed sandy beaches on the Cayenne promontory becoming entirely mud-bound during bank phases [74,76], as in 2015. In extreme cases, mudflat accretion, and even mangrove colonization, can occur in front of these beaches, favoured, especially during near tides, by enhanced wave dissipation [76]. These beaches not only provide a recreation outlet for the city of Cayenne but are also important marine turtle-nesting sites.

While the foregoing discussion has explored the various influences of the tide, especially in terms of the neap–spring and ebb–high tide variations, these variations are instrumental in the appearance of two zones in the study area that exhibit reverse patterns. The coastal zone is characterized by important mud transport rates during the rainy season and a north-northwestward current is observed at the back of the outer part of the bank, especially during neap tides. The estuary, in contrast, exhibits low velocity values for neap conditions that contrast with the maximum values observed in the coastal area. These observed differences underscore the complex interplay of tidal influences on sediment transport and dynamics within the study area, highlighting the need for further exploration to refine the understanding of these patterns.

5. Conclusions

Knowledge of the processes at play in the complex sedimentary dynamics that characterize the interactions between Amazon-derived mud banks and estuaries along the Guianas coast is still very incomplete because in situ studies are difficult to carry out in such an environment. Modelling, therefore, offers a crucial avenue for advancing our understanding of these processes and their potential impact on coastal management. Our study has highlighted the importance of different forcing dynamics in the sediment transport patterns in the study area, and the predicted patterns provide new insights on the sediment dynamics in this complex coastal zone, influenced by Amazon mud. Mudbank migration has been identified as occurring primarily during the rainy season due to sediment transport flux between the back of the bank and the leading edge and as predominantly ebb-driven. This constitutes the fundamental mechanism of mudbank migration on this coast. The spatial and temporal (seasonal) patterns associated with the processes driving its mechanism are, in turn, important in gauging the impacts of mud transport, sedimentation, and erosion on coastal activities. Understanding sedimentation zones is crucial for maintaining navigation channels and managing shorelines. Beaches with mud deposits are protected from wave-induced erosion and provide potential habitats for mangrove development [25]. Our results reflect a coastal configuration with a mud bank located near the mouth. However, how sediment dynamics evolve after the mud bank has passed or during the interbank period still needs further investigation.

To further investigate the interactions between a mud bank and the estuary it migrates across, other important processes, such as stratification [28], river discharge fluctuations, mud consolidation, fluidization, integration of sandy material, or solitary waves [31], need to be considered in future 3D simulations on longer timescales (annual and above). More efforts are also needed to better describe the wave propagation near the shore and inside the estuary [77].This should improve the results and provide deeper insights into the processes involved in estuarine dynamics and mudbank migration in this particular setting. The current study has focused on one estuary with a quasi-steady mud bank location (year 2015) and mainly in the nearshore area. Although the focus has been on the Mahury andconcernsa quasi-steady mud bank (given the low migration accomplished in a year), the results shed light on the dynamics of Guiana estuaries, a class representative of estuaries

significantly influenced by a distant alongshore sediment source. It would be interesting to apply the proposed methodology to other types of Guiana estuaries with deltaic mouths or mouths diverted westward (e.g., [27]) in order to further analyze how the influence of the alongshore migration of the mud bank may vary.

Author Contributions: The authors of thisarticle confirm that neither the manuscript nor any parts of its content are currently under consideration for or published in another journal. All the authors have contributed substantially to the realization of this manuscript and the individual contribution of each of the authors is as follows: conceptualization, N.A.-Z. and N.H.; methodology, N.A.-Z. and N.H.; software, N.A.-Z. and N.H.; validation, N.A.-Z., N.H. and S.O.; formal analysis, N.A.-Z. and N.H.; investigation, N.A.-Z. and N.H.; resources, A.G., N.H. and V.V.; data curation, N.A.-Z. and N.H.; writing—original draft preparation, N.A.-Z. and N.H.; writing—review and editing, N.A.-Z., N.H., V.V., S.O., E.A. and A.G.; visualization, N.A.-Z.; supervision, N.H., V.V. and A.G.; project administration, N.H., V.V. and A.G.; and funding acquisition, N.H., V.V. and A.G. All the authors have approved the final submission. All authors have read and agreed to the published version of the manuscript.

Funding: This work was supported by the co-funding of N. Abascal-Zorrilla's PhD thesis by CNES under the HARDECOT TOSCA project, DEAL Guyane, and Grand Port Maritime de Guyane. Financial support for this work was also provided by the European Regional Development Fund through the project OYAMAR (FEDER/2016/N°188).

Data Availability Statement: Data available on request from the corresponding author.

Acknowledgments: The authors thank the Phares et Balises Service of French Guiana and the DEAL agency of French Guiana for providing data on bathymetry, waves, river discharge, and tides. The authors also thank SHOM for the bathymetric data. This is a contribution of the French GDR LIGA researcher network.

Conflicts of Interest: The authors declare no conflicts of interest.

References

1. Anthony, E.J. The muddy tropical coast of West Africa from Sierra Leone to Guinea- Bissau: Geological heritage, geomorphology and sediment dynamics. *Afr. Geosci. Rev.* **2006**, *13*, 227–237.
2. Chapman, V.J. *Salt Marshes and Salt Deserts of the World*; Academic Press: Cambridge, MA, USA, 1974; pp. 3–19.
3. Lugo, A.E.; Snedaker, S.C. The ecology of mangroves. *Annu. Rev. Ecol. Syst.* **1974**, *5*, 39–64. [CrossRef]
4. Wong, Y.S.; Tam, N.F. Asia-Pacific Symposium on Mangrove Ecosystems. In Proceedings of the International Conference held at the Hong Kong University of Science & Technology, Hong Kong, China, 1–3 September 1993; Springer Science & Business Media: Berlin/Heidelberg, Germany, 1995; Volume 106, p. 1993.
5. Dyer, K.R.; Evans, E.M. Dynamics of Turbidity Maximum in a Homogeneous Tidal Channel. *J. Coast. Res.* **1989**, 23–30.
6. Dalrymple, R.W.; Choi, K. Morphologic and facies trends through the fluvial-marine transition in tide-dominated depositional systems: A schematic framework for environmental and sequence stratigraphic interpretation. *Earth-Sci. Rev.* **2007**, *81*, 135–174. [CrossRef]
7. Wolanski, E.; Spagnol, S. Dynamics of the turbidity maximum in King Sound, tropical Western Australia. *Estuar. Coast. Shelf Sci.* **2003**, *56*, 877–890. [CrossRef]
8. Flemming, B.W.; Delafontaine, M.T.; Liebezeit, G. (Eds.) *Muddy Coast Dynamics and Resource Management*; Elsevier: Edinburgh, UK, 2000; Volume 2.
9. Healy, T. *Muddy Coasts of Mid-Latitude Oceanic Islands on an Active Plate Margin—New Zealand*; Elsevier: Edinburgh, UK, 2002.
10. Anthony, E.J.; Gardel, A.; Zainescu, F.B.G. Fine sediment systems. In *Reference Module in Earth Systems and Environmental Sciences*; Elsevier: Edinburgh, UK, 2021.
11. Wells, J.T.; Coleman, J.M. *Longshore Transport of Mud by Waves: Northeastern Coast of South America*; Coastal Studies Institute, Center for Wetland Resources, Louisiana State University: Baton Rouge, LA, USA, 1978.
12. Allison, M.A.; Lee, M.T.; Ogston, A.S.; Aller, R.C. Origin of Amazon mudbanks along the northeastern coast of South America. *Mar. Geol.* **2000**, *163*, 241–256. [CrossRef]
13. Warne, A.G.; Meade, R.H.; White, W.A.; Guevara, E.H.; Gibeaut, J.; Smyth, R.C.; Aslan, A.; Tremblay, T. Regional controls on geomorphology, hydrology, and ecosystem integrity in the Orinoco Delta, Venezuela. *Geomorphology* **2002**, *44*, 273–307. [CrossRef]
14. Eisma, D.; Augustinus, P.G.E.F.; Alexander, C. Recent and subrecent changes in the dispersal of Amazon mud. *Neth. J. Sea Res.* **1991**, *28*, 181–192. [CrossRef]
15. Augustinus, P.G.E.F. The Changing Shoreline of Surinam (South America). Ph.D. Thesis, Utrecht University, Utrecht, The Netherlands, 1978.

16. Anthony, E.J.; Gardel, A.; Gratiot, N.; Proisy, C.; Allison, M.A.; Dolique, F.; Fromard, F. The Amazon-influenced muddy coast of South America: A review of mud-bank-shoreline interactions. *Earth-Sci. Rev.* **2010**, *103*, 99–121. [CrossRef]
17. Gardel, A.; Gratiot, N. A Satellite Image–Based Method for Estimating Rates of Mud Bank Migration, French Guiana, South America. *J. Coast. Res.* **2005**, *214*, 720–728. [CrossRef]
18. Abascal Zorrilla, N.; Vantrepotte, V.; Gensac, E.; Huybrechts, N.; Gardel, A. The Advantages of Landsat 8-OLI-Derived Suspended Particulate Matter Maps for Monitoring the Subtidal Extension of Amazonian Coastal Mud. *Remote Sens.* **2018**, *10*, 1733. [CrossRef]
19. Froidefond, J.M.; Pujos, M.; Andre, X. Migration of mud banks and changing coastline in French Guiana. *Mar. Geol.* **1988**, *84*, 19–30. [CrossRef]
20. Gratiot, N.; Gardel, A.; Anthony, E.J. Trade-wind waves and mud dynamics on the French Guiana coast, South America: Input from ERA-40 wave data and field investigations. *Mar. Geol.* **2007**, *236*, 15–26. [CrossRef]
21. Winterwerp, J.C.; de Graaff, R.F.; Groeneweg, J.; Luijendijk, A.P. Modelling of wave damping at Guyana mud coast. *Coast. Eng.* **2007**, *54*, 249–261. [CrossRef]
22. Zhu, S.; Wei, W.; Zhu, Q.; Wan, K.; Xing, F.; Yan, W.; Gao, J.; Wang, Y. Wave attenuation and transformation across a highly turbid muddy tidal flat-salt marsh system. *Appl. Ocean Res.* **2024**, *147*, 103980. [CrossRef]
23. Liu, X.; Lu, Y.; Yu, H.; Ma, L.; Li, X.; Li, W.; Zhang, H.; Bian, C. In-Situ Observation of Storm-Induced Wave-Supported Fluid Mud Occurrence in the Subaqueous Yellow River Delta. *J. Geophys. Res. Ocean.* **2022**, *127*, 1–19. [CrossRef]
24. Safak, I.; Sheremet, A.; Davis, J.; Kaihatu, J.M. Nonlinear wave dynamics in the presence of mud-induced dissipation on Atchafalaya Shelf, Louisiana, USA. *Coast. Eng.* **2017**, *130*, 52–64. [CrossRef]
25. Toorman, E.A.; Anthony, E.; Augustinus, P.G.E.F.; Gardel, A.; Gratiot, N.; Homenauth, O.; Huybrechts, N.; Monbaliu, J. Interaction of Mangroves, Coastal Hydrodynamics, and Morphodynamics Along the Coastal Fringes of the Guianas. In *Threats to Mangrove Forests*; Springer: Berlin/Heidelberg, Germany, 2018; Volume 20, ISBN 9783319730165.
26. Anthony, E.J.; Gardel, A.; Gratiot, N. *Fluvial Sediment Supply, Mud Banks, Cheniers and the Morphodynamics of the Coast of South America between the Amazon and Orinoco River Mouths*; Geological Society London Special Publications: London, UK, 2013. [CrossRef]
27. Gardel, A.; Anthony, E.J.; Ferreira dos Santos, V.; Huybrechts, N.; Lesourd, S.; Sottolichio, A.; Maury, T. A remote sensing-based classification approach for river mouths of the Amazon-influenced Guianas coast. *Reg. Environ. Chang.* **2022**, *22*, 65. [CrossRef]
28. Orseau, S.; Lesourd, S.; Huybrechts, N.; Gardel, A. Hydro-sedimentary processes of a shallow tropical estuary under Amazon influence. The Mahury Estuary, French Guiana. *Estuar. Coast. Shelf Sci.* **2017**, *189*, 252–266. [CrossRef]
29. Orseau, S.; Abascal Zorrilla, N.; Huybrechts, N.; Lesourd, S.; Gardel, A. Decadal-scale morphological evolution of a muddy open coast. *Mar. Geol.* **2020**, *420*, 106048. [CrossRef]
30. Walcker, R.; Gratiot, N.; Anthony, E.J. Remote Sensing-based Monitoring of the Muddy Mangrove Coastline of French Guiana. In *Land Surface Remote Sensing in Urban and Coastal Areas*; Elsevier: Edinburgh, UK, 2016; pp. 297–320. [CrossRef]
31. Chevalier, C.; Baklouti, M.; Ramamonjiarisoa, A. Modeling the influence of wind and rivers on current, salinity and temperature over the French Guiana continental shelf during the rainy season. *J. Coast. Res.* **2004**, *20*, 1183–1197. [CrossRef]
32. Bourret, A.; Devenon, J.L.; Chevalier, C. Tidal influence on the hydrodynamics of the French Guiana continental shelf. *Cont. Shelf Res.* **2008**, *28*, 951–961. [CrossRef]
33. Chevalier, C.; Froidefond, J.M.; Devenon, J.L. Numerical analysis of the combined action of littoral current, tide and waves on the suspended mud transport and on turbid plumes around French Guiana mudbanks. *Cont. Shelf Res.* **2008**, *28*, 545–560. [CrossRef]
34. Rodriguez, H.N.; Mehta, A.J. Modelling muddy coast response to waves. *J. Coast. Res.* **2001**, *27*, 137–148.
35. Kranenburg, W.M.; Winterwerp, J.C.; de Boer, G.J.; Cornelisse, J.M.; Zijlema, M. SWAN-Mud, an engineering model for mud-induced wave-damping. *J. Hydraul. Eng.* **2011**, *137*, 959–975. [CrossRef]
36. Rogers, W.E.; Holland, K.T. A study of dissipation of wind-waves by mud at Cassino Beach, Brazil: Prediction and inversion. *Cont. Shelf Res.* **2009**, *29*, 676–690. [CrossRef]
37. Adesina, R.B.; He, Z.; Oladejo, H.O.; Dada, O.A.; Ajibade, H.J. High-resolution wave modeling of the Southwestern Nigerian coastal shelf: Implications on geomorphic contrasts between barrier-lagoon and mud coasts. *Mar. Geol.* **2024**, *470*, 107253. [CrossRef]
38. Ng, C.-O. Water waves over a muddy bed: A two layer Stokes' boundary layer model. *Coast. Eng.* **2000**, *40*, 221–242. [CrossRef]
39. Dalrymple, R.A.; Liu, P.L.F. Waves over soft muds: A two-layer fluid model. *J. Phys. Oceanogr.* **1978**, *8*, 1121–1131. [CrossRef]
40. Do, A.T.; Sottolichio, A.; Huybrechts, N.; Gardel, A. Circulation pattern and implication for fine sediment transport in a preserved tropical estuary: The case of the Maroni (French Guiana). *Reg. Stud. Mar. Sci.* **2020**, *40*, 101493. [CrossRef]
41. Lisboa, P.V.; Fernandes, E.H.; Sottolichio, A.; Huybrechts, N.; Bendô, A.R.R.; Costi, J. Bottom evolution patterns driven by hydrodynamic forcing in the Southwest Atlantic Inner Continental Shelf, off Río de la Plata and Patos Lagoon. *Cont. Shelf Res.* **2023**, *255*, 104934. [CrossRef]
42. Parvathy, K.G.; Bhaskaran, P.K. Nearshore modelling of wind-waves and its attenuation characteristics over a mud dominated shelf in the Head Bay of Bengal. *Reg. Stud. Mar. Sci.* **2019**, *19*, 100665. [CrossRef]
43. Anthony, E.J.; Gardel, A.; Proisy, C.; Fromard, F.; Gensac, E.; Peron, C.; Walcker, R.; Lesourd, S. The role of fluvial sediment supply and river-mouth hydrology in the dynamics of the muddy, Amazon-dominated Amapá-Guianas coast, South America: A three-point research agenda. *J. S. Am. Earth Sci.* **2013**, *44*, 18–24. [CrossRef]

44. Abascal, N. Dynamics of the Amazonian Mud Bank System through Spatial Observation and Hydro-Sedimentary Modeling: Application to the Coastal Domain of French Guiana. Ph.D. Thesis, Université de Guyane, Cayenne, France, 2019.
45. Pujos, M.; Latouche, C.; Maillet, N. Late Quaternary paleoceanography of the French Guiana continental shelf: Clay-mineral evidence. *Oceanol. Acta* **1996**, *19*, 477–489.
46. Augustinus, P.G.E.F. The influence of the trade winds on the coastal development of the Guianas at various scale levels: A synthesis. *Mar. Geol.* **2004**, *208*, 145–151. [CrossRef]
47. Lasserre, J.; Collinet, M. *Base Navale de Degrad des Cannes (Cayenne)—Etude Hydrodynamique et Sedimentologique*; Phase i. Technical Report RP-52541-FR; BRGM: Orléans, France, 2003.
48. Baklouti, M.; Devenon, J.L.; Bourret, A.; Froidefond, J.M.; Ternon, J.F.; Fuda, J.L. New insights in the French Guiana continental shelf circulation and its relation to the North Brazil Current retroflection. *J. Geophys. Res. Ocean.* **2007**, *112*, 1–18. [CrossRef]
49. Babin, M.; Morel, A.; Fournier-Sicre, V.; Fell, F.; Stramski, D. Light scattering properties of marine particles in coastal and open ocean waters as related to the particle mass concentration. *Limnol. Oceanogr.* **2003**, *48*, 843–859. [CrossRef]
50. Abascal Zorrilla, N.; Vantrepotte, V.; Ngoc, D.D.; Huybrechts, N.; Gardel, A. Automated SWIR based empirical sun glint correction of Landsat 8-OLI data over coastal turbid water. *Opt. Express* **2019**, *27*, 294–318. [CrossRef]
51. Han, B.; Loisel, H.; Vantrepotte, V.; Mériaux, X.; Bryère, P.; Ouillon, S.; Dessailly, D.; Xing, Q.; Zhu, J. Development of a Semi-Analytical Algorithm for the Retrieval of Suspended Particulate Matter from Remote Sensing over Clear to Very Turbid Waters. *Remote Sens.* **2016**, *8*, 211. [CrossRef]
52. McFeeters, S.K. The use of the Normalized Difference Water Index (NDWI) in the delineation of open water features. *Int. J. Remote Sens.* **1996**, *17*, 1425–1432. [CrossRef]
53. Wu, G.; Wang, K.; Liang, B.; Wu, X.; Wang, H.; Li, H.; Shi, B. Modeling the morphological responses of the Yellow River Delta to the water-sediment regulation scheme: The role of impulsive river floods and density-driven flows. *Water Resour. Res.* **2023**, *59*, e2022WR033003. [CrossRef]
54. Egbert, G.D.; Erofeeva, S.Y. Efficient inverse modeling of barotropic ocean tides. *J. Atmos. Ocean. Technol.* **2002**, *19*, 183–204. [CrossRef]
55. Roche, M.; Dubreuil, P.; Hoepffner, M. Dynamique des eaux, des Sels et des Sediments en Suspension dans les Estuaires du Mahury et de l'Approuague:etude en vue de L'alimentation D'une Usine de Pate de Bois (Guyane française). 1974. Available online: https://www.paralia.fr/jngcgc/15_33_sottolichio.pdf (accessed on 29 September 2024).
56. Orseau, S. Dynamique Sédimentaire d'un Estuaire Tropical Sous Influence Amazonienne: Le cas de l'estuaire du Mahury. Ph.D. Thesis, University du Littoral Cote d'Opale, Dunkerque, France, 2016.
57. Bi, Q.; Toorman, E.A. Mixed-sediment transport modelling in Scheldt estuary with a physics-based bottom friction law. *Ocean. Dyn.* **2015**, *65*, 555–587. [CrossRef]
58. Tassi, P.; Villaret, C. *Sisyphe User's Manual*; Report EDF LNHE (H-P74-2012-02004-EN); EDF: Paris, France, 2014; Volume 33, p. 74.
59. Partheniades, E. A Study of Erosion and Deposition of Cohesive Soils in Salt Water. Ph.D. Thesis, University of California, Los Angeles, CA, USA, 1962.
60. Périgaud, C. Mécanique de l'érosion des vases. *Houille Blanche* **1983**, *69*, 501–512. [CrossRef]
61. Gratiot, N.; Anthony, E.J. Role of flocculation and settling processes in development of the mangrove-colonized, Amazon-influenced mud-bank coast of South America. *Mar. Geol.* **2016**, *373*, 1–10. [CrossRef]
62. Migniot, C.; Hamm, L. Consolidation and rheological properties of mud deposits. *Coast. Eng.* **1990**, 2975–2983. [CrossRef]
63. Wang, Z.; Liang, B.; Wu, G.; Borsje, B.W. Modeling the formation and migration of sand waves: The role of tidal forcing, sediment size and bed slope effects. *Cont. Shelf Res.* **2019**, *190*, 103986. [CrossRef]
64. van der Westhuysen, A.J.; Zijlema, M.; Battjes, J.A. Nonlinear saturation-based whitecapping dissipation in SWAN for deep and shallow water. *Coast. Eng.* **2007**, *54*, 151–170. [CrossRef]
65. Battjes, J.A.; Janssen, J.P.F.M. Energy loss and set-up due to breaking of random waves. *Coast. Eng.* **1978**, *1978*, 569–587.
66. Vantrepotte, V.; Gensac, E.; Loisel, H.; Gardel, A.; Dessailly, D.; Mériaux, X. Satellite assessment of the coupling between in water suspended particulate matter and mud banks dynamics over the French Guiana coastal domain. *J. S. Am. Earth Sci.* **2013**, *44*, 25–34. [CrossRef]
67. Allison, M.A.; Lee, M.T. Sediment exchange between Amazon mudbanks and shore-fringing mangroves in French Guiana. *Mar. Geol.* **2004**, *208*, 169–190. [CrossRef]
68. Fiot, J.; Gratiot, N. Structural effects of tidal exposures on mudflats along the French Guiana coast. *Mar. Geol.* **2006**, *228*, 25–37. [CrossRef]
69. Gensac, E.; Gardel, A.; Lesourd, S.; Brutier, L. Morphodynamic evolution of an intertidal mudflat under the influence of Amazon sediment supply—Kourou mud bank, French Guiana, South America. *Estuar. Coast. Shelf Sci.* **2015**, *158*, 53–62. [CrossRef]
70. Gardel, A.A.; Gensac, E.; Anthony, E.J.; Lesourd, S.; Loisel, H.; Marin, D.; Gardel, A.; Gensac, E.; Anthony, E.J.; Lesourd, S.; et al. Wave-formed mud bars: Their morphodynamics and role in opportunistic mangrove colonization. *J. Coast. Res.* **2011**, *64*, 384–387.
71. Froidefond, J.M.; Lahet, F.; Hu, C.; Doxaran, D.; Guiral, D.; Prost, M.T.; Ternon, J.F. Mudflats and mud suspension observed from satellite data in French Guiana. *Mar. Geol.* **2004**, *208*, 153–168. [CrossRef]
72. Anthony, E.J.; Dolique, F.; Gardel, A.; Gratiot, N.; Proisy, C.; Polidori, L. Nearshore intertidal topography and topographic-forcing mechanisms of an Amazon-derived mud bank in French Guiana. *Cont. Shelf Res.* **2008**, *28*, 813–822. [CrossRef]

73. Vantrepotte, V.; Loisel, H.; Mériaux, X.; Neukermans, G.; Dessailly, D.; Jamet, C.; Gensac, E. Seasonal and inter-annual (2002–2010) variability of the suspended particulate matter as retrieved from satellite ocean color sensor over the French Guiana coastal waters. *J. Coast. Res.* **2011**, *64*, 1750–1754.
74. Anthony, E.J.; Gardel, A.; Dolique, F.; Guiral, D. Short-term changes in the plan shape of a sandy beach in response to sheltering by a nearshore mud bank, Cayenne, French Guiana. *Earth Surf. Process. Landf.* **2002**, *866*, 857–866. [CrossRef]
75. Brunier, G.; Fleury, J.; Anthony, E.J.; Gardel, A.; Dussouillez, P. Close-range airborne Structure-from-Motion Photogrammetry for high-resolution beach morphometric surveys: Examples from an embayed rotating beach. *Geomorphology* **2016**, *261*, 76–88. [CrossRef]
76. Anthony, E.J.; Dolique, F. The influence of Amazon-derived mud banks on the morphology of sandy headland-bound beaches in Cayenne, French Guiana: A short- to long-term perspective. *Mar. Geol.* **2004**, *208*, 249–264. [CrossRef]
77. Gao, J.; Hou, L.; Liu, Y.; Shi, H. Influences of bragg reflection on harbor resonance triggered by irregular wave groups. *Ocean Eng.* **2024**, *305*, 117941. [CrossRef]